Journal of Theoretical Biology 479 (2019) 73–80

Contents lists available at ScienceDirect

Journal of Theoretical Biology

journal homepage: www.elsevier.com/locate/jtb

A chemotaxis-based explanation of spheroid formation in 3D cultures of breast cancer cells

Federica Bubba[a,1], Camille Pouchol[a,1], Nathalie Ferrand[b], Guillaume Vidal[c], Luis Almeida[a,*], Benoît Perthame[a], Michèle Sabbah[b]

[a] Sorbonne Université, CNRS, Université de Paris, Inria, Laboratoire Jacques-Louis Lions, 4 pl. Jussieu, Paris 75005, France
[b] Sorbonne Université, INSERM, Laboratoire de Biologie du Cancer et Thérapeutique, Centre de Recherche Saint-Antoine, Paris 75012, France
[c] CELENYS, Biopolis 2, 75 route de Lyons-la-forêt, Rouen 76000, France

ARTICLE INFO

Article history:
Received 15 October 2018
Revised 24 May 2019
Accepted 3 July 2019
Available online 5 July 2019

MSC:
35B36
35Q92
62P10
97M60

Keywords:
Mathematical biology
Keller–Segel
Pattern formation
Linear stability analysis

ABSTRACT

Three-dimensional cultures of cells are gaining popularity as an *in vitro* improvement over 2D Petri dishes. In many such experiments, cells have been found to organize in aggregates. We present new results of three-dimensional *in vitro* cultures of breast cancer cells exhibiting patterns. Understanding their formation is of particular interest in the context of cancer since metastases have been shown to be created by cells moving in clusters. In this paper, we propose that the main mechanism which leads to the emergence of patterns is chemotaxis, *i.e.*, oriented movement of cells towards high concentration zones of a signal emitted by the cells themselves. Studying a Keller–Segel PDE system to model chemotactical auto-organization of cells, we prove that it admits Turing unstable solutions under a time-dependent condition. This result is illustrated by two-dimensional simulations of the model showing spheroidal patterns. They are qualitatively compared to the biological results and their variability is discussed both theoretically and numerically.

Introduction

In breast cancer, the majority of deaths are not due to the primary tumor itself but are the result of the ability of cancer cells to migrate and colonize other organs in the body, *i.e.*, to form metastases (Nguyen et al., 2009). Even when they are few, highly motile tumor cells are able to move and spread throughout the entire body, but it is now well established that cancer cells creating metastases typically move in clusters and not alone (Aceto et al., 2014; Hong et al., 2016). Moreover, organs most usually affected by breast cancer metastases, such as lungs, bones and liver, produce proteins which attract chemokine receptors in cancerous cells (Müller et al., 2001). The migrative properties of cells and their chemotactic abilities, *i.e*, their directing movement towards zones of high concentration of certain chemical stimuli, are thus key when it comes to understanding the development of metastases in breast cancer. Over the past decades, the *in vitro* investigation of how cells move and organize in the extracellular matrix (ECM) has developed thanks to the design of 3D structures mimicking the ECM, see (Haycock, 2011) for a review of the different engineering techniques. The typical behavior of cells cultured inside these is aggregation (Lee et al., 2008), creating patterns whose characteristics depend on the cell line (Kenny et al., 2007; Singh et al., 2016). Cells aggregated into clusters might have a selective advantage over single cells thanks to their ability to escape the immune response, facilitating the extravasation, while it might prevent anoikis (the programmed death of cells detached from the ECM), see (Friedl and Wolf, 2003; Jurasz et al., 2004; Zhao et al., 2010). In this paper, we are interested in determining the main biological phenomenon responsible for the formation of cellular aggregates through mathematical modeling. Models for the aggregative behavior of cells in the ECM are well developed and belong to two main classes: discrete (or agent-based) models, where each cell is represented individually (Drasdo and Höhme, 2005; Schlüter et al., 2012; Zhou et al., 2006), or continuous models typically based on ordinary differential equations (ODEs) or partial differential equations (PDEs) (Anderson, 2005; Painter et al., 2010). The latter can be either phenomenological or derived from physical or chemical laws as outlined in (Painter, 2009), where patterning is

* Corresponding author.
E-mail addresses: luis@ann.jussieu.fr, luis.almeida@sorbonne-université.fr (L. Almeida).
[1] These authors contributed equally to this work.

https://doi.org/10.1016/j.jtbi.2019.07.002
0022-5193/

obtained but requires anisotropy assumptions on the ECM. Patterns are also reported in 2D Petri dishes in various cases such as buds created by glioblastoma cells. In (Agosti et al., 2019), such experimental results are presented together with a PDE mechanical model which is shown to numerically reproduce aggregates. To the best of our knowledge, however, works on the formation of patterns by cells in the ECM or in artificial 3D structures do not incorporate chemical environmental cues inducing chemotaxis. In a deterministic setting, the latter phenomenon is commonly modeled thanks to the Keller–Segel system (Keller and Segel, 1970) or one of its numerous generalizations (Hillen and Painter, 2009). Originally employed to model spatial patterns in bacteria populations, this model has been shown to be a rich tool for the modeling of self-organization phenomena (Painter, 2018). This work provides new experimental results of spheroidal aggregates created by cancerous cells in a 3D hydrogel. It proposes a chemotaxis-based explanation of patterns through theoretical and numerical analysis of Turing instabilities exhibited by a Keller–Segel-type PDE model.

The outline of the paper is as follows. In Section 1, we present the experimental results and the main features of their PDE-based counterpart. In Section 2, we introduce the full model, whose linear stability analysis is performed in Section 3. Numerical simulations of the model are given in Section 4, and we conclude by discussing the results and possible improvements in Section 5.

1. From experimental to modeling results

In this Section, we report new results of experiments exhibiting spheroidal patterns, specifically for breast cancer cells growing in a 3D cylindrical hydrogel, of radius 2.5 mm and height 2 mm. Cells are put at the top of the structure and, after spreading uniformly, have typically formed spheroids no later than the day 4 (D4) of culture. This is true both for an epithelial cell line (MCF7) and a more mesenchymal and invasive one (MCF7-sh-wisp2), although patterns appear to be more regular in the first cell line and exhibit more elongated shapes with geometric variability in the second, see Fig. 1.

A typical spheroid has a radius of around 100 µm, and thus can be estimated to contain about 5 000 cells. As reported on Fig. 2, at D4 spheroids have appeared for both cell lines and for most number of seeded cells, which varies from 10 000 to 100 000. Interestingly, almost no spheroids are observed at low initial number of cells in the MCF7-sh-wisp2 case. We also note that the number of spheroids is about the same for 50 000 or 75 000 seeded cells. Finally, very few spheroids are observed at 100 000 initial cells. This last observation should be handled with care since it is essentially the effect of cells tending to escape and pack outside the hydrogel. Thus, 100 000 might be a too high initial number of cells for the experiment to run properly.

Building on these experiments, we propose that chemotaxis (along with diffusion and growth) is the driving force behind the emergence of these patterns. In our case, well-documented chemoattractants are the chemokines CXCL12 and CXCL8, mostly expressed by MCF7 cells and MCF7-sh-wisp2 cells respectively (Sabbah et al., 2011). To support our claim, we provide a minimally-parametrized variant of the Keller–Segel system with prevention of overcrowding. Even if for the initial number of cells we consider in the biological experiments (from about 10^4 to 10^5) an agent-based version of the Keller–Segel model could still be feasible and possibly more accurate, we will study here the PDE-based version. This choice not only enables deeper analysis of the patterning mechanism but also becomes more and more appropriate as cells grow, since their number doubles every day.

In agreement with the biological observation that cells have quickly spread uniformly, we consider a homogeneous initial condition, starting from which the system has an exponentially growing homogeneous time-dependent solution, driven by the growth of cells.

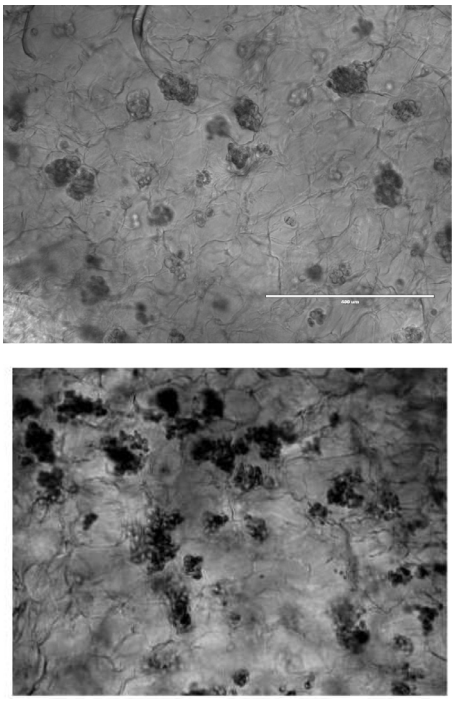

Fig. 1. 2D image of spheroids in the hydrogel, formed by MCF7 cells (upper panel) and by cells from MCF7-sh-wisp2 (lower panel), in both cases for 75 000 seeded cells and after 4 days of culture.

We investigate Turing instabilities for this model around the time-dependent spatially-homogeneous solution. Assuming that the time-scale of growth is long compared to that of kinetics, we prove that such instabilities exist under a time-dependent necessary and sufficient condition, which we call $IC(t)$. The instability condition provides us with a dynamical explanation of patterns:

- as long as $IC(t)$ is not satisfied, the solution evolves close to the homogeneous solution,
- when $IC(t)$ starts being fulfilled, patterns arise on the quick time scale of kinetics.

We discuss in detail and compare to experiments the dependence of $IC(t)$ on the initial number of cells and on the parameter for the invasiveness of cells. Most experimental results are shown to be coherent with the theoretical predictions, and they justify the nonlinearity chosen in the Keller–Segel system. Remaining mismatches are also analyzed and put in perspective with the minimality of our model.

Finally, we provide 2D simulations for the equations in a disk, which both confirm our theoretical claims and show a qualitative match with experimental data. We investigate the relevance of these 2D simulations when it comes to patterning, by proving that patterns in the 2D disk provide a good approximation for their three-dimensional counterpart in a cylinder, when the cylinder height is relatively small compared to its radius. Since the hydrogel we used in the experiments does not satisfy this smallness assumption, we detail this result in the Appendix because of its independent interest.

1.1. Materials and methods

A schematic view of the experimental process is given in Fig. 3. It consists in the 3D culture of specific breast cancer cell lines using hydrogel 96-low binding microwell arrays (Biomimesys) de-

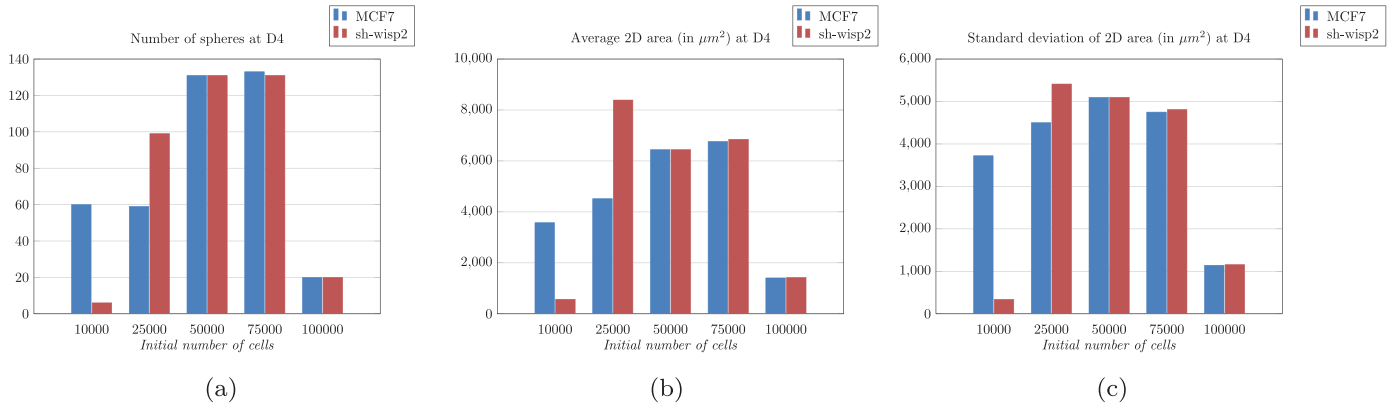

Fig. 2. Statistics of spheroids formed in the hydrogel by MCF7 and MCF7-sh-wisp2 cells after 4 days of culture: number of spheres (A), mean and standard deviation of sizes of spheroids (B) and (C), both as a function of the number of seeded cells. Statistics obtained by averaging the results of 5 randomly chosen images in a given hydrogel.

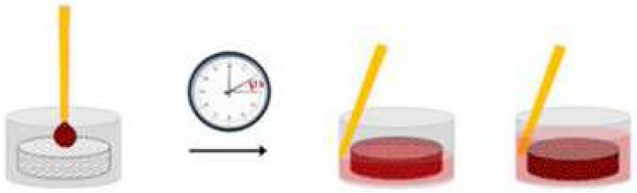

Fig. 3. Experimental process of micro-tumor formation: cells are suspended on the top center of the hydrogel 96-well-plates in a humidified atmosphere containing 5% CO_2, at 37°C. After 1 h of incubation, 150 µl of medium is added in the space between the well and the hydrogel.

veloped by Celenys. Cells counted and suspended in 50 µl of medium were seeded at different densities, from 10 000 to 100 000 cells/well. Medium was changed every 2 days during the whole experiment, and when the spheres became too big, the hydrogels (containing spheres) were placed in 24-well-plates to keep supplying nutrients to the cells.

Two breast cell lines were used for this study: MCF7 (human breast cell line, epithelial phenotype) and MCF7-sh-WISP2 (MCF7 cells invalidated for WISP2 by sh-RNA plasmid, mesenchymal phenotype, (Ferrand et al., 2014; Fritah et al., 2008)). Cells were routinely maintained in Dulbecco's modified Eagle medium supplemented with 10% fetal bovine serum (FBS), L-Glutamine, and antibiotics. Live-cell microscopy imaging of spheroids was obtained by using EVOS microscope (EVOS Cell Imaging System, Thermofisher). Images were collected with either $\times 4$ or $\times 10$ objectives depending on the sizes of spheroids after 4 days of culture. Image analysis was carried out using the freely available ImageJ software. Spheroids were analyzed by using either defined (round or oval selection) or freehand selections.

2. Mathematical model

The Keller–Segel system describes the biased random motion of cells towards a chemical stimulus, called chemoattractant. We consider two variants which take into account volume effects. The equation is posed on a domain $\Omega \subset \mathbb{R}^d$ with $d = 2$ or $d = 3$. We shall consider the case of a cylinder in $\mathbb{R}^3$ to match the hydrogel geometry and for the simulations we consider a disk in $\mathbb{R}^2$. We are interested in the Keller–Segel system of parabolic reaction-diffusion equations that writes

$$\begin{cases} \frac{\partial n}{\partial t} - D_1 \Delta n + \chi \nabla \cdot (\varphi(n) \nabla c) = r\, n, \\ \frac{\partial c}{\partial t} - D_2 \Delta c = \alpha n - \beta c, \end{cases} \tag{1}$$

where $n(t, x)$ is the density of the population of cancer cells and $c(t, x)$ is the concentration of the chemoattractant, for $x \in \Omega$ and $t > 0$.

We impose no-flux boundary conditions at the boundary $\partial\Omega$

$$\begin{cases} (D_1 \nabla n - \chi \varphi(n) \nabla c) \cdot \mathbf{n} = 0, \\ D_2 \nabla c \cdot \mathbf{n} = 0, \end{cases}$$

where $\mathbf{n}$ is the outward unit normal at the boundary. With this choice, cells and chemoattractant neither leave nor enter the domain. We complete this system with nonnegative initial conditions $n(0, x) = n^0(x)$ and $c(0, x) = c^0(x)$ and we define the average initial mass

$$M := \frac{1}{|\Omega|} \int_\Omega n^0(x) dx.$$

2.1. Model description

The second equation in (1) describes the dynamics of the concentration of the chemoattractant $c(t, x)$: it diffuses at rate $D_2 > 0$, is produced by the cells themselves at rate $\alpha > 0$ and is naturally degraded at rate $\beta > 0$. Cells diffuse at a constant rate $D_1 > 0$ and grow according to a linear law with intrinsic rate r. Not only does this choice ease computations, but we argue it is an appropriate description of the phase before the emergence of patterns, since cells have much space to grow and nutrients are brought to them constantly.

Finally, the random diffusive movement is complemented with a transport term in the direction of the gradient of chemoattractant c. The constant $\chi > 0$ measures the strength of motion and $\varphi(n)$, called "chemotactical sensitivity function", is a nonlinear function describing the way cells aggregate when following the chemical signal. We shall consider either

$$\varphi(n) = n\left(1 - \frac{n}{n_{\max}}\right)_+ \quad \text{or} \quad \varphi(n) = n\, e^{-\frac{n}{n_{\max}}},$$

where x_+ stands for the positive part of a given real number x and $n_{\max}$ plays the role of a critical density above which the chemotactical movement respectively vanishes or becomes negligible with respect to diffusion. Density-dependent sensitivity functions have been considered in various works such as (Hillen and Painter, 2001; 2002). Note that one could also think of a flux-limited Keller–Segel where the gradient is premultiplied by a nonlinear function of its norm as in (Perthame et al., 2018), but we stick to the simpler model above. We will show that a nonlinear choice of the sensitivity function is necessary for a correct agreement between theoretical predictions and experimental results.

Remark 2.1. Because of the linear growth for the cellular population, the critical density $n_{\max}$ will eventually be exceeded, in which case a nonlinearity $\varphi(n) = n(1 - \frac{n}{n_{\max}})$ would not make sense since cells would go in the direction given by $-\nabla c$. This explains our choice with the positive part which completely shuts down any chemotactic movement above the maximal density $n_{\max}$.

As observations show, cells quickly spread uniformly in the 3D structure and we start after this spreading phase: we assume

$$n^0(x) \equiv M, \quad c^0(x) \equiv \frac{\alpha}{\beta} M,$$

where M is defined above and represents (up to the scaling factor $\frac{1}{|\Omega|}$) the initial number of cells seeded in the 3D structure.

2.2. Dimensionless model

Upon changes of time and space variables $\tilde{t} = \beta \frac{D_1}{D_2} t$, $\tilde{x} = \sqrt{\frac{\beta}{D_2}} x$ and appropriate scalings for n and c, namely

$$n(t,x) = \tilde{n}\left(\beta \frac{D_1}{D_2} t, \sqrt{\frac{\beta}{D_2}} x\right),$$
$$c(t,x) = \frac{\alpha}{\beta} \tilde{c}\left(\beta \frac{D_1}{D_2} t, \sqrt{\frac{\beta}{D_2}} x\right), \tag{2}$$

and writing again n for $\tilde{n}$, c for $\tilde{c}$ we find a minimally parametrized version:

$$\begin{cases} \frac{\partial n}{\partial t} - \Delta n + A \nabla \cdot (\varphi(n) \nabla c) = r_0 n, \\ \varepsilon \frac{\partial c}{\partial t} - \Delta c = n - c. \end{cases} \tag{3}$$

Only three parameters A, ε and r_0 now remain, given by

$$A = \frac{\alpha \chi}{\beta D_1}, \quad \varepsilon = \frac{D_1}{D_2}, \quad r_0 = \frac{r}{\beta \varepsilon}.$$

We expect A to be larger for MCF7-sh-wisp2 cells than for MCF7 cells, the former being more prone to chemotactic movement than the latter (Fritah et al., 2008; Sabbah et al., 2011).

Small Parameters: Because the chemoattractant diffuses much faster than cells, ε is typically small, while A depends on the ratio $\frac{\chi}{D_1}$, which measures the relative importance of diffusion and attraction.

We also assume that the time scale of growth (driven by r) is much bigger than the time scale of kinetics (driven by α, β). Thus, r_0 is much smaller than $\frac{1}{\varepsilon}$. The MCF7 cells indeed have a population doubling time of around 1 day (Sutherland et al., 1983), which yields $r \approx 4.10^{-6}\, s^{-1}$, while some data can be found in the literature on the degradation rate of the chemokine CXCL8, of the order of $\beta \approx 1.10^{-4}\, s^{-1}$ (Shi et al., 1995). Summing up, we assume both

$$\varepsilon \ll 1, \qquad r_0 \varepsilon = \frac{r}{\beta} \ll 1. \tag{4}$$

Note that $r_0 \varepsilon = \frac{r}{\beta} \approx 4.10^{-2}$ is arguably not very small, but we will see later on that our results actually hold up to $\mathcal{O}((r_0\varepsilon)^2)$ errors, see Remark 3.1, and $(r_0\varepsilon)^2 \approx 2.10^{-3}$.

For the homogeneous initial condition $n^0 = M$, $c^0 = \frac{\alpha}{\beta} M$, this system has a homogeneous (in space) solution, given by

$$\bar{n}(t) := M e^{r_0 t},$$
$$\bar{c}(t) := \frac{M}{1 + \varepsilon r_0}\left(\frac{\alpha(1 + \varepsilon r_0) - \beta}{\beta} e^{-\frac{t}{\varepsilon}} + e^{r_0 t}\right),$$

the (linear) stability of which we now investigate in detail.

3. Linear stability analysis

Around the homogeneous solution $(\bar{n}(t), \bar{c}(t))$, the linearized system reads

$$\begin{cases} \frac{\partial n}{\partial t} - \Delta n + A\varphi(\bar{n}(t))\Delta c = r_0 n, \\ \varepsilon \frac{\partial c}{\partial t} - \Delta c = n - c. \end{cases} \tag{5}$$

We denote $(\psi_k)_{k \geq 1}$ the orthonormal basis of $L^2(\Omega)$ made of the eigenfunctions of the Neumann Laplace operator associated with eigenvalues $(\lambda_k)_{k \geq 1}$, namely

$$\begin{cases} -\Delta \psi_k = \lambda_k \psi_k, & x \in \Omega \\ \nabla \psi_k \cdot \mathbf{n} = 0, & x \in \partial\Omega. \end{cases}$$

Since biological experiments have been performed in 3D cylinders, we explicitly compute the modes of Neumann Laplace in Appendix A for this geometry, where we also remark that perturbations along the $z-$axis will typically not be observed if the height of the cylinder were to be negligible with respect to its radius.

Projecting the linearized Eq. (5) on the orthonormal basis $(\psi_k)_{k \geq 1}$ through

$$n(t,\cdot) = \sum a_k(t)\psi_k, \; c(t,\cdot) = \sum b_k(t)\psi_k,$$

we find

$$\begin{cases} a_k'(t) = -\lambda_k a_k(t) + A\varphi(\bar{n}(t))\lambda_k b_k(t) + r_0 a_k(t), \\ \varepsilon b_k'(t) = -\lambda_k b_k(t) + a_k(t) - b_k(t). \end{cases}$$

The previous equation writes in matrix form as $X_k'(t) = A_k(t) X_k(t)$ with

$$X_k(t) = \begin{pmatrix} a_k(t) \\ b_k(t) \end{pmatrix}, \; A_k(t) = \begin{pmatrix} -\lambda_k + r_0 & A\varphi(\bar{n}(t))\lambda_k \\ \frac{1}{\varepsilon} & -\frac{1}{\varepsilon}(\lambda_k + 1) \end{pmatrix}.$$

We now assume that the perturbation is initiated at time $t_0 > 0$ and we focus on an interval of the form $(t_0, t_0 + \Delta t)$ whose size Δt is of the order of the kinetics time-scale ε. As such, it is small when compared to the growth time-scale $\frac{1}{r_0}$. Note that in the original time variable, this amounts to considering a time interval of order $\frac{1}{\beta}$ (small when compared to $\frac{1}{r}$). In particular, neglecting terms of order $\mathcal{O}((r_0\varepsilon))$, we can approximate all functions of time by their value at t_0.

Looking for exponentially increasing solutions in time, we insert a solution of the form

$$(a_k(t), b_k(t)) = e^{\mu(t - t_0)}(a_k^0, b_k^0),$$

with μ of real part $\Re(\mu) > 0$, which imposes that μ is an eigenvalue of $A_k(t)$. Let us denote $\mu_k^+(t)$ to be either the largest real eigenvalue of $A_k(t)$ or the real part of its complex conjugate eigenvalues.

We now look for sufficient and necessary conditions ensuring that $\mu_k^+(t) > 0$.

For a given time $t > 0$, we compute

$$\mathrm{Tr}(A_k(t)) = -\lambda_k + r_0 - \frac{1}{\varepsilon}(\lambda_k + 1) \leq r_0 - \frac{1}{\varepsilon} < 0.$$

It is thus easy to check that $A_k(t)$ has an eigenvalue with positive real part if and only if $\det(A_k(t)) < 0$, which is equivalent to

$$-\lambda_k^2 + (A\varphi(\bar{n}(t)) + r_0 - 1)\lambda_k + r_0 > 0.$$

Since we are interested in perturbations other than those in the direction of the first homogeneous eigenfunction ψ_1 (and since the above polynomial is positive at 0), a necessary and sufficient condition to have $\mu_k^+(t) > 0$ is for $\lambda_k > 0$ to satisfy

$$\lambda_k < \bar{\lambda}(t)$$

where

$$\bar{\lambda}(t) := \frac{r_0+A\varphi(\bar{n}(t))-1+\sqrt{(r_0+A\varphi(\bar{n}(t))-1)^2+4r_0}}{2}.$$

In other words, looking for perturbations in a direction other than that of the eigenfunction ψ_1 which is homogeneous, a perturbation at time t_0 will yield Turing instability if and only if

$$\lambda_2 < \bar{\lambda}(t_0), \tag{6}$$

neglecting small terms in $\mathcal{O}((r_0\varepsilon))$. As in the Introduction, we call this condition $IC(t_0)$.

Remark 3.1. If one replaces $\bar{\lambda}(t_0)$ by $\bar{\lambda}(t_0+\frac{\Delta t}{2})$ in the previous condition, the instability condition can be proved to be accurate not only at order 0 but even at order 1 in $r_0\,\varepsilon$, *i.e.*, neglecting $\mathcal{O}((r_0\varepsilon)^2)$ corrections, see (Madzvamuse et al., 2010).

The perturbations happen along the modes ψ_k which for simple geometries as in our case can be explicitly computed, see Appendix A.

3.1. On the condition for Turing instability

In condition (6), the right-hand side $\bar{\lambda}(t)$ has the same monotonicity as φ as a function of $\bar{n}(t_0) = Me^{r_0 t_0}$. Recall that the function φ increases and then decreases in both cases $\varphi(n) = n\left(1-\frac{n}{n_{\max}}\right)_+$ and $\varphi(n) = ne^{-\frac{n}{n_{\max}}}$.

3.1.1. Dependence on time

Assume that M is fixed such that initially, $\varphi(\bar{n}(t))$ increases with time (*i.e.*, $\varphi'(M)>0$). Consequently, the condition $IC(t)$ in (6) might not initially be satisfied but it is more likely to be as time increases. The typical dynamics expected from this condition is thus an increase of $n(t,\cdot)$, $c(t,\cdot)$ very close to $\bar{n}(t)$, $\bar{c}(t)$, up until the Turing instability condition becomes satisfied. Patterns then form very quickly (on the time scale of ε).

3.1.2. Dependence on the initial mass

For a small initial mass M, the right-hand side in condition $IC(t)$ in (6) is small, meaning that Turing instabilities are expected only at a large time t. This provides an explanation for the fact that patterns are not initially observed. In the limit when M is very small, one should wait for a very long time before $IC(t)$ starts being satisfied.

As M increases, Turing instability is more likely to occur before D4, until the cell density reaches the region in which φ decreases. When M is too large, $IC(t)$ is not satisfied initially and will never be later on: no patterns should be obtained. This in accordance with experimental observations, and explains why we choose a nonlinear sensitivity function instead of the more classical linear one. A linear choice would indeed predict Turing instabilities for high values of M.

3.1.3. Dependence on the parameter A

We note that the dependence of $IC(t)$ in (6) as a function of A is such that if $IC(t)$ is satisfied at some time t for a given A, then it should be for a larger A as well. In other words, if MCF7 cells have created patterns at day D4, then so should have the MCF7-sh-wisp2 (all other parameters being equal). This is not in agreement with the experimental findings with $M = 10\,000$, value for which MCF7 cells have created spheroids, but not MCF7-sh-wisp2. We however stress that predictions of our continuum PDE model should be taken with care when dealing with the lowest possible densities and first days of experiment.

4. Numerical simulations

In this section, we complete the theoretical analysis with numerical simulations of system (3) showing how the patterning behavior of solution changes depending only on few parameters, as commented in the previous sections. All simulations have been performed with the software Freefem++, which is based on finite element methods (Hecht, 2012). They have been carried out on a circular domain of radius $R = 20$, discretized with at least 500 points mesh.

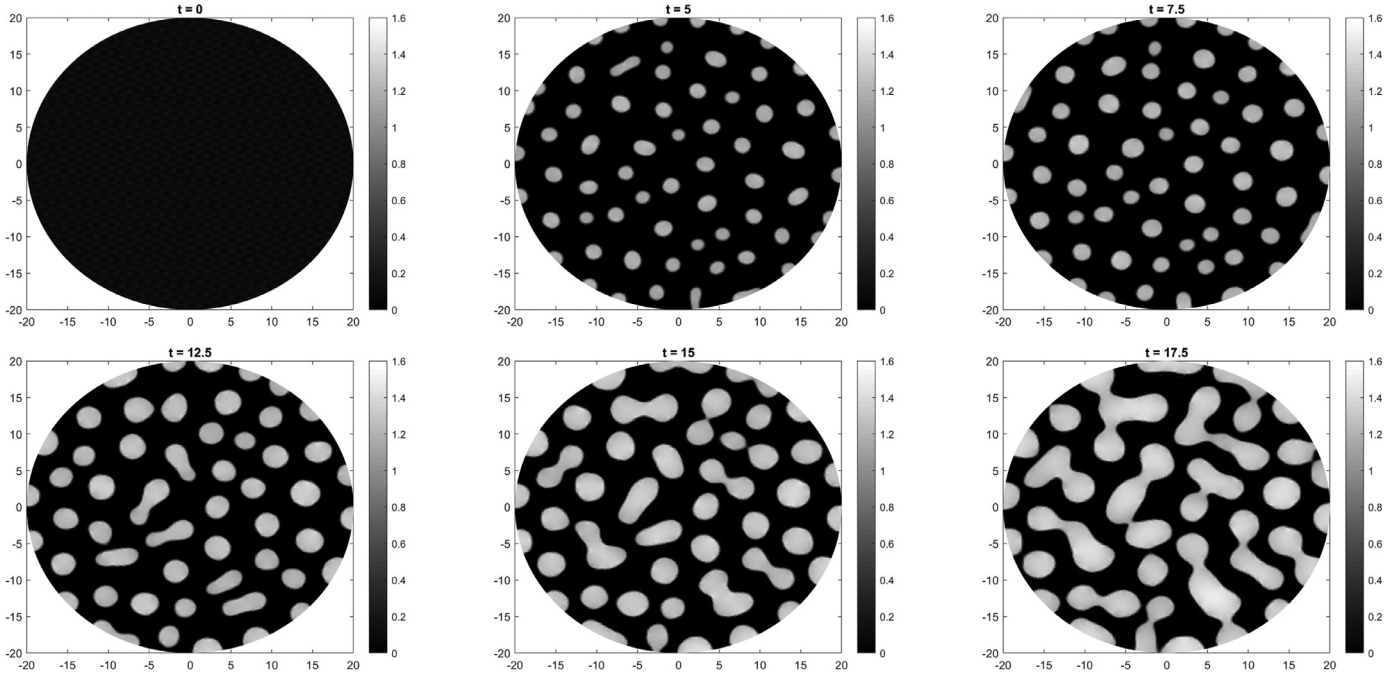

Fig. 4. Patterning evolution. Evolution of the density of cells from a small perturbation of the initial uniform state $n_0 = 0.1$ ($t = 0$). Here, $\varphi(n) = n(1-n)_+$, $A = 70$, $\varepsilon = 0.01$ and $r_0 = 0.1$.

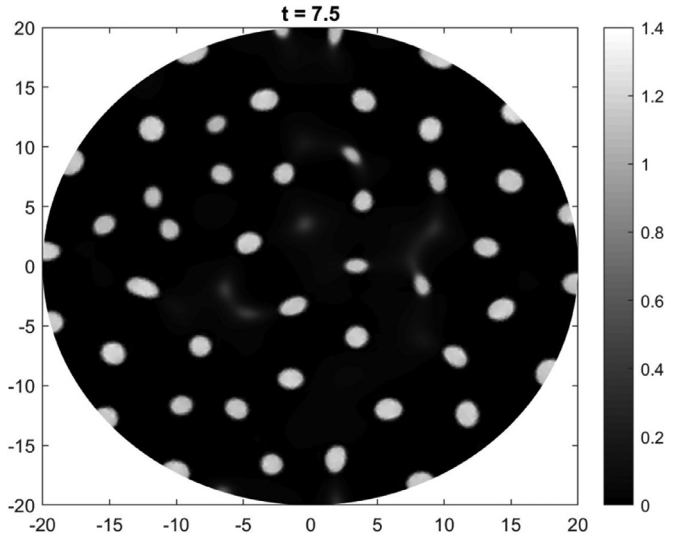

Fig. 5. Patterns appear around time $t = 7.5$ when $n_0 = 0.05$, $A = 70$, $\varepsilon = 0.01$ and $r_0 = 0.1$.

4.1. Typical behavior

When the parameters are such that they are near the instability region (6), the typical behavior of the solutions is the one showed in Fig. 4, where we set $A = 70$, $\varepsilon = 0.01$, $r_0 = 0.1$ and used the logistic chemotactical sensitivity function with $n_{\max} = 1$, *i.e.*, $\varphi(n) = n(1-n)_+$. Starting from a small perturbation of the constant initial distribution $n_0 = 0.1$, in few time steps the density grows uniformly in the domain until $IC(t)$ in (6) is satisfied, in this case around $t \approx 2.5$. Pattern formation then occurs very quickly, compared to the growth dynamics. When patterns are formed, the solution evolves very slowly and the most visible phenomenon is the merging of the spheroidal aggregates. Eventually, they become less regular, round structures, as at $t = 17.5$.

4.2. Dependence on the initial mass

If the initial mass is too small, the initial phase of growth takes much longer and the patterns arise later. For example in Fig. 5, where the solution of the model with the initial distribution value $n_0 = 0.05$ (leaving all the other parameters unchanged) is displayed, the first patterns appear only around $t \approx 7.5$.

4.3. Dependence on the parameter A

In Fig. 6, we show how the kind of patterns observed strongly depends on the value of the quantity χ/D_1. In these simulations, we chose $A = 200$ and the other parameters as in Fig. 4. In this case the diffusivity of cells is not as strong as the chemotactical attraction, which dominates the dynamics leading to smaller but more numerous spheroids. Moreover, in the first phases of dynamics, slightly more non-spheroidal and of variable geometry patterns arise.

4.4. Choice of the function φ

Finally, Fig. 7 shows solutions of the system (3) with $\varphi(n) = ne^{-n}$. For this chemotactical sensitivity function, we find again spheroidal aggregates, but with less variable structures: in this case, variability lies in the maximums of the solution (higher than the ones in the logistic case), but only very round aggregates can be observed.

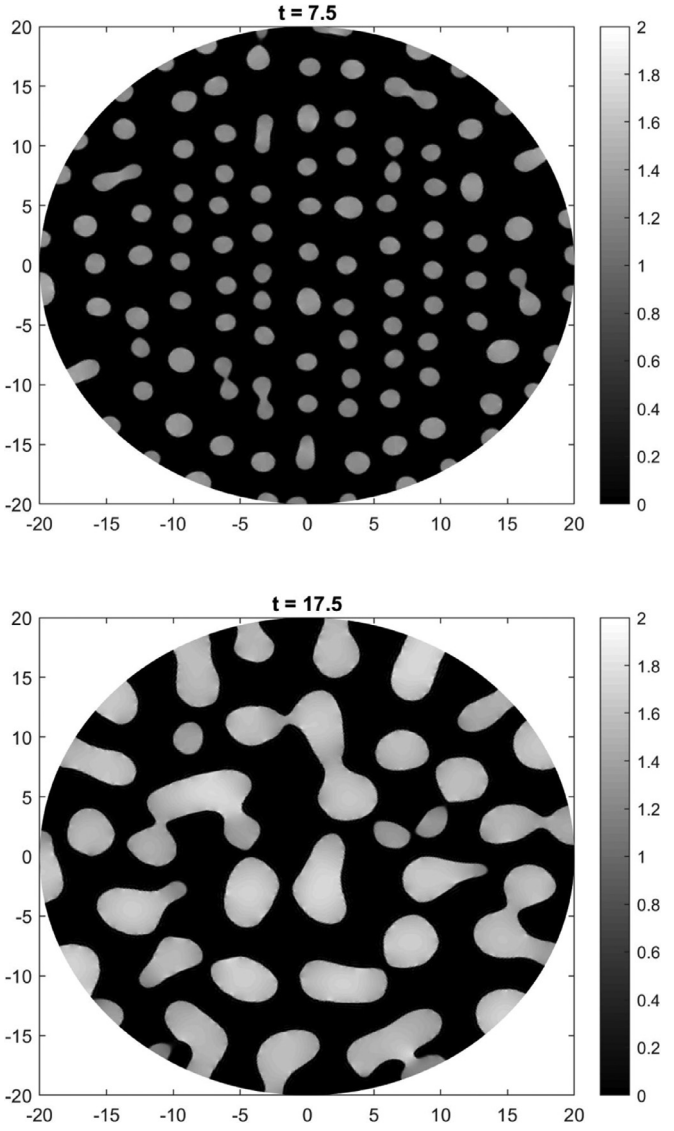

Fig. 6. Evolution of the density of cells from a small perturbation of the initial uniform state $n_0 = 0.1$, with $\varphi(n) = n(1-n)_+$, $A = 200$, $\varepsilon = 0.01$ and $r_0 = 0.1$.

While the exponential function is usually advocated for because it does not impose an *a priori* maximal density, we here highlight a drawback of this choice: since the packing can continue even at high density, this fixes the size of patterns as new cells do not go at the periphery but instead concentrate at higher and higher density at the middle. Thus, this choice of function offers less variability for the size of spheroids in two dimensions.

Note that the numerical schemes do not preserve desirable properties, such as positivity of the solution. In fact, negative values in the densities can be seen mostly at the interfaces between zones of high densities (the spheroids), and zones of low densities (the rest). We were able to take fine enough grids to limit these numerical artifacts but we point out that some positivity-preserving numerical schemes have been designed to solve systems of the type of (1), see for example (Almeida et al., 2019) and (Liu et al., 2018).

5. Discussion and conclusions

In order to understand the experimental observation of spheroidal aggregates in cultures of breast cancer cells, we have proposed a mathematical model which includes a chemotactic ef-

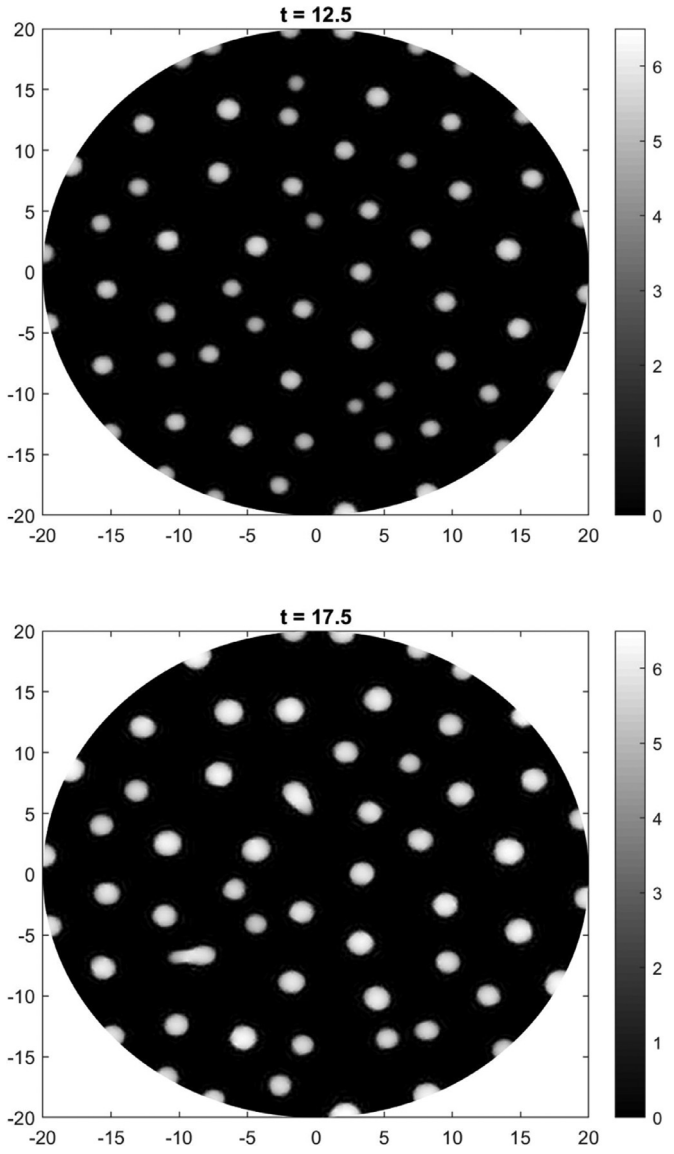

Fig. 7. Alternative model. Evolution of the density of cells from the initial state $n_0 = 0.1$ in the case where $\varphi(n) = ne^{-n}$. All parameters have been chosen as in Fig. 4.

fect and its modulation at high cell densities. We have analyzed theoretically the conditions which lead to instability and pattern formation. The numerical solutions confirm the theoretical analysis and qualitatively reproduce the observed patterns, in spite of its relatively low parametrization. Contrarily to other modeling approaches, the salient feature is not cell-scaffold adhesion, which we reduce to a constant diffusion term, but instead chemotaxis. We thus hypothesize that it is a key phenomenon responsible for these aggregates.

The numerical simulations of the model do not only show qualitative accordance with the experimental results. Indeed, the system (1) has spatially inhomogeneous solutions with spheroidal patterns, and it also describes how different kinds of patterns can arise: few, elongated structures for a small diffusion value or numerous, mainly round, small aggregates for a stronger chemotactic sensitivity.

The simplicity of the model induces two main limitations:

- it does not seem to offer a satisfying flexibility for the size of patterns, essentially fixed by the geometry of Ω.
- it is not suitable to explain the post-aggregation phase, and in particular the increase in the number of spheres as observed experimentally 10 days after initial pattern formation.

In fact, the distributions (in size) of spheroids for the biological images and the numerical simulations do not match well: while the standard deviation is of the order of the average size for experiments as evidenced by Fig. 2 in the Introduction, we find that standard deviation is about one third of the mean size in simulations.

In the Keller–Segel model, the variability is essentially captured only by the Laplacian eigenfunctions which themselves are completely characterized by the domain geometry. A natural direction of research for a better matching is to model cell-scaffold adhesion more finely than with a diffusion term, incorporating anisotropies (such as in Painter, 2009), or even randomness, in the extracellular matrix density.

As for the second point, statistical estimates obtained from images taken later during the experiment (not shown here) indeed evidence a growth in both the size and number of spheroids. This is not reproduced by numerical simulations. In fact, the patterns that formed then typically continue to merge, probably until the cells are all packed in very few aggregates. This phenomenon for this type of model is explained in detail in (Potapov and Hillen, 2005).

We insist that a minimally-parametrized model such as ours is more amenable to mathematical analysis and also paves the way for works aiming at a more quantitative prediction of the typical size and number of spheroids. To go further in this direction, one should look for the actual modes along which instabilities will be observed in a time-dependent setting, in the spirit of Madzvamuse et al. (2010).

Acknowledgment

The authors acknowledge partial funding from the ANR blanche project Kibord ANR-13-BS01-0004 funded by the French Ministry of Research. B.P. has received funding from the European Research Council (ERC) under the European Union's Horizon 2020 research and innovation program (grant agreement No 740623). F.B. has received funding for international mobility from Universit Franco-italienne.

Appendix A. Explicit computation of the modes

Since Ω has a particular shape, eigenvalues and eigenfunctions can actually be explicitly computed. We first consider the case of the 2D simulations, namely when Ω is a disk of radius a. It is then standard that all eigenfunctions can be obtained after separation of variables in polar coordinates $\psi(x, y) = f(r)g(\theta)$, the equation $-\Delta\psi = \lambda\psi$ with Neumann boundary conditions is equivalent to

$$g(\theta) = A\cos(m\theta) + B\sin(m\theta)$$

for some $m \in \mathbb{Z}$ and $\rho \mapsto f(\frac{\rho}{\sqrt{\lambda}})$ must solve the Bessel equation

$$\rho^2 y''(\rho) + \rho y'(\rho) + (\rho^2 - m^2)y(\rho) = 0$$

with $y'(0) = y'(\sqrt{\lambda}a) = 0$. This yields, up to a constant, to the result $f(r) = J_m(\sqrt{\lambda}r)$ where J_m is the first kind Bessel function of order m. The boundary conditions impose $m \neq \pm 1$ (because $J'_m(0) = 0$ for all m except 1 and -1), while, denoting $\gamma_{m,p}$ the pth zero of the derivative of J_m, we find $\lambda = \left(\frac{\gamma_{m,p}}{a}\right)^2$.

Summing up, we obtain

$$\lambda_{m,p} = \left(\frac{\gamma_{m,p}}{a}\right)^2,$$

$$\psi_{m,p}(r, \theta) = J_m\left(\frac{\gamma_{m,p}}{a}r\right)(A\cos(m\theta) + B\sin(m\theta)),$$

a family indexed by $m \in \mathbb{Z} \setminus \{\pm 1\}$, $p \in \mathbb{N}^\star$. Apart from $m = 0$ for which the eigenfunction is unique after normalisation, the eigenspace associated to $\lambda_{m,p}$ is of dimension 2.

Similar computations for the case of a cylinder of height h and radius a lead to the result

$$\lambda_{m,p,l} = \left(\frac{\gamma_{m,p}}{a}\right)^2 + \left(\frac{l\pi}{h}\right)^2,$$

$$\psi_{m,p,l}(r,\theta,z) = \psi_{m,p}(r,\theta)\cos\left(\frac{l\pi z}{h}\right),$$

a family indexed by $m \in \mathbb{Z} \setminus \{\pm 1\}$, $p \in \mathbb{N}^\star$, $l \in \mathbb{N}$. The multiplicity of eigenfunctions is the same as in the previous case (1 if $m = 0$ and 2 if not).

If h is small compared to a, the contribution of the $(\frac{l\pi}{h})^2$ term is too big and we will thus typically not see the eigenvalues such that $l > 0$ in the z variable, an approximation precise up to $\mathcal{O}((\frac{a}{h})^2)$ errors. As a consequence, only the corresponding modes for $l = 0$ will be observed, and we note that these are exactly the 2D modes.

Under this smallness assumption, it is interesting to note that from the point of view of Turing instabilities, it is a good approximation to neglect the z variable and focus on $\Omega \subset \mathbb{R}^2$ as a disk.

References

Aceto, N., Bardia, A., Miyamoto, D.T., Donaldson, M.C., et al., 2014. Circulating tumor cell clusters are oligoclonal precursors of breast cancer metastasis. Cell 158 (5), 1110–1122.

Agosti, A., Marchesi, S., Scita, G., Ciarletta, P., 2019. The self-organised, non-equilibrium dynamics of spontaneous cancerous buds arXiv:0902.0885.

Almeida, L., Bubba, F., Perthame, B., Pouchol, C., 2019. Energy and implicit discretization of the Fokker–Planck and Keller–Segel type equations. Netw. Heterog. Media 14 (1), 23–41.

Anderson, A.R.A., 2005. A hybrid mathematical model of solid tumour invasion: the importance of cell adhesion. Math. Med. Biol. 22 (2), 163–186.

Drasdo, D., Höhme, S., 2005. A single-cell-based model of tumor growth in vitro: monolayers and spheroids. Phys. Biol. 2 (3), 133–147.

Ferrand, N., Gnanapragasam, A., Dorothee, G., Redeuilh, G., et al., 2014. Loss of WISP2/CCN5 in estrogen-dependent MCF7 human breast cancer cells promotes a stem-like cell phenotype. PloS One 9 (2).

Friedl, P., Wolf, K., 2003. Tumour-cell invasion and migration: diversity and escape mechanisms. Nat. Rev. Cancer 3 (5), 362–374.

Fritah, A., Saucier, C., De Wever, O., Bracke, M., et al., 2008. Role of WISP-2/CCN5 in the maintenance of a differentiated and noninvasive phenotype in human breast cancer cells. Mol. Cell Biol. 28 (3), 1114–1123.

Haycock, J.W., 2011. 3D cell culture: a review of current approaches and techniques. Methods Mol. Biol. 695, 1–15.

Hecht, F., 2012. New development in freefem++. J. Comput. Math. 20, 251–266.

Hillen, T., Painter, K.J., 2001. Global existence for a parabolic chemotaxis model with prevention of overcrowding. Adv. Appl. Math. 26, 280–301.

Hillen, T., Painter, K.J., 2002. Volume-filling and quorum-sensing in models for chemosensitive movement. Can. Appl. Math. Q. 10 (4), 501–543.

Hillen, T., Painter, K.J., 2009. A user's guide to PDE models for chemotaxis. J. Math. Biol. 58, 183–217.

Hong, Y., Fang, F., Zhang, Q., 2016. Circulating tumor cell clusters: what we know and what we expect. Int. J. Oncol. 49 (6), 2206–2216.

Jurasz, P., Alonso-Escolano, D., Radomski, M.W., 2004. Platelet-cancer interactions: mechanisms and pharmacology of tumour cell induced platelet aggregation. Br. J. Pharmacol. 143, 819–826.

Keller, E.F., Segel, L.A., 1970. Initiation of slime mold aggregation viewed as an instability. J. Theor. Biol. 26, 399–415.

Kenny, P.A., Lee, G.Y., Myers, C.A., Neve, R.M., et al., 2007. The morphologies of breast cancer cell lines in three-dimensional assays correlate with their profiles of gene expression. Mol. Oncol. 1 (1), 84–96.

Lee, J., Cuddihy, M.J., Kotov, N.A., 2008. Three-dimensional cell culture matrices: state of the art. Tissue. Eng. Part B Rev. 14 (1), 61–86.

Liu, J.-G., Wang, L., Zhou, Z., 2018. Positivity-preserving and asymptotic preserving method for 2D Keller–Segel equations. Math. Comput. 87 (311), 1165–1189.

Madzvamuse, A., Gaffney, E.A., Maini, P.K., 2010. Stability analysis of non-autonomous reaction-diffusion systems: the effects of growing domains. J. Math. Biol. 61 (1), 133–164.

Müller, A., Homey, B., Soto, H., Ge, N., et al., 2001. Involvement of chemokine receptors in breast cancer metastasis. Nature 410.

Nguyen, D.X., Bos, P.D., Massague, J., 2009. Metastasis: from dissemination to organ-specific colonization. Nat. Rev. Cancer 9, 274–284.

Painter, K.J., 2009. Modelling cell migration strategies in the extracellular matrix. J. Math. Biol. 58.

Painter, K.J., 2018. Mathematical models for chemotaxis and their applications in self-organisation phenomena. J. Theor. Biol.

Painter, K.J., Armstrong, N.J., Sherratt, J.A., 2010. The impact of adhesion on cellular invasion processes in cancer and development. J. Theor. Biol. 264 (3), 1057–1067.

Perthame, B., Vauchelet, N., Wang, Z., 2018. The flux limited Keller–Segel system; properties and derivation from kinetic equations arXiv:1801.07062.

Potapov, A.B., Hillen, T., 2005. Metastability in chemotaxis models. J. Dyn. Differ. Equ. (2) 293–330.

Sabbah, M., Prunier, C., Ferrand, N., Megalophonos, V., et al., 2011. CCN5, a novel transcriptional repressor of the transforming growth factor β signaling pathway. Mol. Cell. Biol. 31, 1459–1469.

Schlüter, D.K., Ramis-Conde, I., Chaplain, M., 2012. Computational modeling of single-cell migration: the leading role of extracellular matrix fibers. Biophys. J. 103 (6), 1141–1151.

Shi, M.M., Godleski, J.J., Paulauskis, J.D., 1995. Molecular cloning and post-transcriptional regulation of macrophage inflammatory protein-1α in alveolar macrophages. Biochem. Biophys. Res. Commun. 211 (1), 289–295.

Singh, M., Mukundan, S., Jaramillo, M., Oesterreich, S., Sant, S., 2016. Three-dimensional breast cancer models mimic hallmarks of size-induced tumor progression. Cancer Res. 76 (13), 3732–3743.

Sutherland, R.L., Hall, R.E., Taylor, I.W., 1983. Cell proliferation kinetics of MCF-7 human mammary carcinoma cells in culture and effects of tamoxifen on exponentially growing and plateau-phase cells. Cancer Res. 43 (9), 3998–4006.

Zhao, Q., Barclay, M., Hilkens, J., Guo, X., et al., 2010. Research interaction between circulating galectin-3 and cancer-associated MUC1 enhances tumour cell homotypic aggregation and prevents anoikis. Mol. Cancer 9.

Zhou, J.J., Coakley, S., Holcombe, M., MacNeil, S., Smallwood, R.H., 2006. Individual cell-based simulation of 3D multicellular spheroid self-assembly. Eur. Cell. Mater. 11.